PHYSICAL REVIEW B **75**, 041405(R) (2007)

Raman intensity mapping of single-walled carbon nanotubes

A. Jungen,[1] V. N. Popov,[2] C. Stampfer,[1] L. Durrer,[1] S. Stoll,[3] and C. Hierold[1]
[1]*Micro and Nanosystems, ETH Zurich, 8092 Zurich, Switzerland*
[2]*Faculty of Physics, University of Sofia, 1164 Sofia, Bulgaria*
[3]*Physical Chemistry Laboratory, ETH Zurich, 8093 Zurich, Switzerland*
(Received 14 October 2006; revised manuscript received 5 December 2006; published 16 January 2007)

We report on the measurement of the Raman intensity of radial breathing modes of a relatively large diameter range of single-walled carbon nanotubes (SWNTs) by confocal Raman scattering. Statistical data analysis yielded an intensity distribution within the excitation width of the single laser line at 2.33 eV. These measurements were compared to recent nonorthogonal tight-binding calculations on the Raman intensity where a match could be found. The mapping allowed for accurate determination of optical transition energies of the nanotubes and their chirality. Higher E_{33}^{M} and E_{55}^{S} optical transitions of both metallic and semiconducting SWNTs could be recorded for which intensity calculations were extended to tube diameters up to 2.6 nm.

DOI: 10.1103/PhysRevB.75.041405 PACS number(s): 78.67.Ch, 73.22.−f, 78.30.Na, 78.66.Tr

The electronic and optical properties of single-walled carbon nanotubes (SWNTs) exhibit a strong dependence on their atomic structure. This dependence is expressed as distinctive one-dimensional energy-level structures which can be experimentally probed by Rayleigh scattering, photoluminescence measurements, and Raman scattering.[1,2] Chirality (n,m) assignment by Raman scattering has been carried out by using tunable laser sources and recording the resonant profiles of the SWNTs.[3–6] Assignment was then performed by overlaying the measured data pairs of the optical transition energies E_{ii} and the radial breathing mode (RBM) frequency ω_{RBM} with calculations in the so-called Kataura plot.[7] Experiments from a range of different quasicontinuous laser excitations resulted in about 50 assignments as reported in Ref. 5. Chirality determination from a single laser line can be less accurate as the fully resonant conditions cannot be determined; thus the difficulty in finding the exact E_{ii} position. Maultzsch *et al.* identified tube families $(2n+m)$ in the same spectrum which were mapped in the Kataura plot from a single excitation.[8]

Recent nonorthogonal tight-binding calculations were extended to provide maximum Raman intensities I_{ii} for each optical transition E_{ii}.[9] However, matching these intensities with measured data has been an experimental challenge. The Raman intensity, in addition to a chirality-dependent scattering efficiency, is strongly dependent on the number of tubes under laser exposure. Furthermore, the orientation of the tubes with respect to the direction of the light polarization affects the Raman intensity.[10] Finally, their length and defects as well as interactions with neighboring tubes can also affect the Raman intensity.[11,12]

We propose a statistical method for measuring the Raman intensity of a nanotube sample using a single laser line by counting the resonant RBM peaks for every measured ω_{RBM}. Given the large amount of data, we obtained the Raman intensity distribution within the excitation linewidth. We then compared the collected data to calculated Raman intensities where a match could be achieved. From this matching the optical transition energies could be determined and chirality assignments could be made.

Individual SWNTs were grown on a SiO_2 substrate by chemical vapor deposition in methane at 900 °C using iron nanoparticles as the catalyst.[13,14] Room temperature Raman spectra were recorded by a WITec CRM 200 device using a green laser line of 532 nm ($E_{\mathrm{L}}=2.33$ eV) which can be focused to a diffraction-limited spot size of about 400 nm (100× objective, numerical aperture 0.8) and recorded in a backscattering geometry through a 50 μm pinhole. The spectrometer was equipped with a Peltier-cooled charge coupled device camera. Precise positioning of the sample under the laser spot was achieved with piezoelectric actuators. Calibration of the system was done as reported elsewhere.[15] 9600 spectra were obtained in six planar scans each collecting 40×40 spectra with an interspot distance of 1 μm at a rate of 2 Hz. RBM features were resolved by fitting each spectrum with Lorentzian lines in the range from 80 to 350 cm^{-1} and normalizing the intensities with respect to the Raman signal from the silicon support (LO phonon at 520 cm^{-1}). Thresholding the fitted peak intensities and widths, for instance, to eliminate the Si feature at 303 cm^{-1} resulted in a selection of 13 743 peaks.

Figure 1(a) shows the fitted Raman intensities as a function of ω_{RBM}. To explain the intensity distribution, we model the measured Raman intensity $I=\varphi(\alpha I_{ii})$ as the product of the intrinsic Raman intensity I_{ii} of a specific SWNT, an attenuation factor $\alpha(\Delta E_{ii})$ taking into account the distance $\Delta E_{ii}=E_{ii}-E_{\mathrm{L}}$ between its fully resonant transition energy and the laser energy, and a factor φ which depends on the experiment. $\varphi=\varphi(\Delta\theta,\Delta r,j)$ is a function of the angle $\Delta\theta$ between the polarization direction and the tube axis, the distance Δr from the (point) scatterer to the center of the laser spot, and the number of identical scatterers j under the same laser spot $(0\leqslant\varphi\leqslant j)$. As sampling is expected to average φ to a constant, the average plot is less noisy than the maximum intensity plot as can be seen in Fig. 1(a). However, fluctuations in the average still correlate with the maximum intensities. We argue that this is because the number of scatterers j under the same laser spot greatly influenced the average plot.

Figure 1(b) shows a histogram of the observed RBM peaks with a 1 cm^{-1} interval width. In order to remove the sample population dependence from the data, we measured

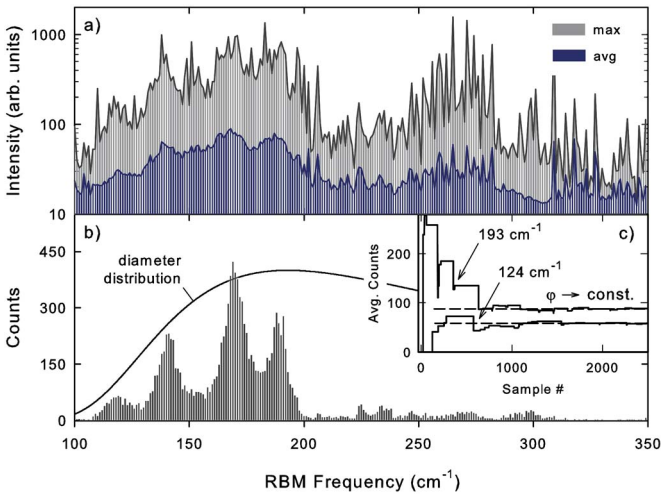

FIG. 1. (Color online) (a) Raman intensity distribution of the measured RBM frequencies. (b) Histogram of the measured Raman intensities and diameter distribution measured by atomic force microscopy. (c) Histogram convergence of average counts of two RBM's upon sampling.

the tube diameter distribution with an atomic force microscope in tapping mode. The obtained measurement was fitted to a Gaussian distribution plotted in Fig. 1(b).[23] The histogram shows four well-resolved features in the range from 100 to 200 cm^{-1}. This is an indication that a selection process from resonant Raman scattering occurred, meaning that for large ΔE_{ii} the Raman intensity is strongly attenuated ($\alpha \ll 1$) from an off-resonance situation. Consider two different SWNTs where $\alpha_1 I_{ii,1} > \alpha_2 I_{ii,2}$. During sampling, both tubes will have produced the same number of counts after population distribution correction; however, as the system only recorded the strongest signals (selection), more counts will have been recorded for tube 1 and the relation $I_1 > I_2$ is preserved. In fact, the Raman system acquired the spectra at a fast rate, and consequently only nanotubes with high scattering efficiency and small ΔE_{ii} contributed to the histogram. By correcting the counts for the diameter distribution, one can thus consider the measure of counts to be a measure of the Raman intensity. The reason why this method seems more powerful than intensity averaging is given by the fact that the individual count is not dependent on the number of scatterers j under the same laser spot. For example, if $j=2$ the recorded intensity may have doubled compared to only one scatterer, but still only one count is attributed to that chirality. Of course, one has to ascertain that the chirality-independent factor φ stabilized after large sampling, which is shown for two selected tubes in Fig. 1(c).

In the following we discuss the intensity mapping between the presented measurement and theoretical calculations. Figure 2(a) shows the optical transition energies as a function of the tube diameter as obtained from our nonorthogonal tight-binding model.[16] The dots shown in red (dark gray) are a selection of optical transitions with high maximum Raman intensity with respect to the laser excitation energy E_L. Tubes lying close to the laser line but still shown in gray have a very weak intrinsic Raman intensity. They are omitted in Fig. 2(b) to avoid figure overloading. To perform such a selection the calculated maximum Raman intensities I_{ii} were multiplied with a Lorentzian function α with center $E_L = 2.33$ eV and width $\Gamma = 0.08$ eV. The value for Γ was first adapted from the literature[12] (0.1 eV) and then empirically fine-tuned to 0.08 eV which provided the best match with the measured data. Figure 2(b) shows the calculated I_{ii} and attenuated Raman intensities αI_{ii} of the selected SWNTs. Figure 2(c) shows the converted histogram from Fig. 1(b). ω_{RBM} was converted to diameter d using the relation $\omega_{RBM} = c_1/d + c_2$ with $c_1 = 214$ cm^{-1} nm and $c_2 = 19$ cm^{-1}. We implicitly account for tube interactions with the c_2 constant.[8] The intensity distribution shows a correlation with the attenuated data from Fig. 2(b). The pattern match is valid only for the attenuated data which underlines the importance of performing such an excitation-dependent correction. Most of the peaks in the histogram did not come from a complete nanotube branch $(2n+m)$ but rather just from the ends of the branches, i.e., from tubes with a large chiral angle.

The identification of SWNT branches through the proposed method allows for chiral assignment. If for a given ω_{RBM} only one E_{ii} lies in the resonance window, the chirality assignment is reasonably unambiguous. However, if several E_{ii} fall in one ω_{RBM}, assignments can be made by mapping

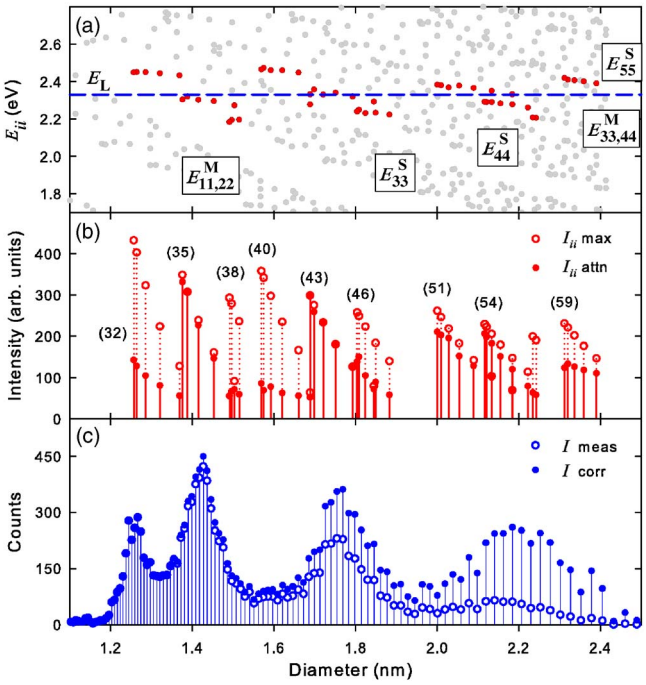

FIG. 2. (Color online) (a) Optical transition energies E_{ii} as a function of the tube diameter. Shown in red (dark gray) are a selection of high-intensity SWNTs with respect to the excitation line of 2.33 eV. The complete set is plotted in the background as a guide to the eye (gray filled circles). All calculated data was rigidly upshifted by 0.43 eV (see text). (b) Calculated Raman intensities corresponding to the selected dots in (a). The open dots are calculated maximum intensities. The filled dots were multiplied with a normal distribution function to model the distance (in eV) to the laser line. Numbers in parentheses indicate tube families $(2n+m)$. (c) Converted measured histogram from Fig. 1(b). The measured data (open circles) were corrected for sample population independence (filled circles). Only large diameters are shown.

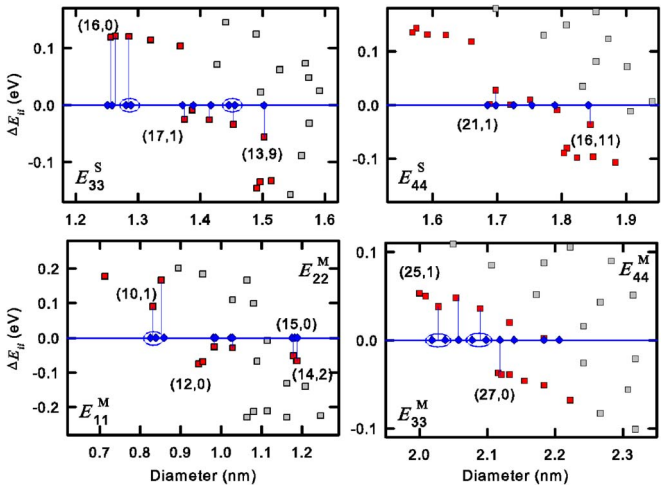

FIG. 3. (Color online) $\Delta E_{ii}=E_{ii}-E_L$ optical transitions of semiconducting (top) and metallic (bottom) SWNTs. Squares indicate calculations [red (dark gray) squares define the resonant window] while diamonds represent measured data from the $\Delta E=0$ line.

the intensity sequence of the chirality candidates on a more tentative basis. Assignment of semiconducting tubes is shown in the top of Fig. 3. Here, we display a selection of measured ω_{RBM} of highest Raman intensity which provided an unambiguous match. Obviously peaks were recorded for any theoretical value; however, we only show peaks that clearly mapped taking care to exclude tentative assignments. As the fitted data were rounded to integers to form a histogram, pairs of measured peaks were eventually collectively attributed to one calculated peak if the attribution situation was safe. It is seen that the observations matched the calculations for the lower parts of the E_{33} and E_{44} branches for tubes with high chiral angle. Tubes with large chiral angle were preferentially mapped; however, we cannot, at this stage, draw any conclusion on the chiral angle distribution in the sample. Table I lists the assigned semiconducting SWNTs. There is a nice agreement between the calculated and measured intensities except for family 43. Higher-order transitions E_{55}^S were observed and assigned [Fig. 2(a)]. Given the low number of counts, their assignment accuracy was reduced. Large diameter tube assignment is affected by the $1/\omega_{RBM}$ relationship to the diameter, explaining the higher error for the (59) tube family as seen in Table I.

Table II lists the assignment for metallic tubes. For E_{11}^M and E_{22}^M transitions, the calculated data were subjected to an upshift of 0.32 eV. The calculated data of higher transitions ($i>2$) were subjected to an upshift of 0.43 eV which is in agreement with Ref. 17. It has been shown that, due to the reduced dimensionality, self-energy and excitonic effects change qualitatively the optical spectra of carbon nanotubes.[18,19] Recently, calculations on exciton properties were shown to exhibit chirality dependencies with a distinct family behavior.[20] For our interpretation of the different upshifts, the lower transition corrections include both self-energy and exciton contributions whereas for the higher transitions only self-energy upshift is essential. These energy corrections, which were initially adapted from the literature, were changed in combination with the c_1, c_2 diameter conversions to detect possible assignment ambiguities; however, cautious examination showed that the provided parameters were optimal and that the match was quite unique. To us, the mapping worked surprisingly well and we cannot exclude that it is the result of a fortuitous cancellation of errors in the calculations. The observation of E_{22}^M (sometimes referred to as E_{11H}^M) transitions had been reported for the first time only

TABLE I. The measured RBM frequency ω_{RBM}, assigned transition energy E_{ii}, calculated and attenuated maximum Raman intensity, and measured Raman intensity of the assigned (n,m) semiconducting SWNTs of the branch $(2n+m)$. ϵ_{rel} represents the relative error between the measured diameter $d=c_1/(\omega_{RBM}-c_2)$ and the theoretical diameter $d=a_0/\pi\sqrt{n^2+nm+m^2}$ with $a_0=2.461$ Å.

ω_{RBM}	E_{ii}	I_{calc}^{max}	I_{calc}^{attn}	I_{meas}^{count}	n	m	Branch	ϵ_{rel} (%)
174	2.31	347	**330**	**330**	17	1	(35) E_{33}^S	0.81
173	2.32	306	**304**	**343**	16	3		0.37
171	2.30	237	**225**	**415**	15	5		0.43
167	2.30	160	**146**	**273**	14	7		0.49
162	2.27	91	**71**	**131**	13	9		0.42
190	2.45	430	**142**	**288**	16	0	(32) E_{33}^S	0.19
189	2.45	401	**128**	**278**	15	2		0.19
185	2.45	322	**105**	**250**	14	4		0.67
146	2.33	298	**298**	**126**	21	1	(43) E_{44}^S	0.06
145	2.36	274	**258**	**113**	20	3		0.19
143	2.33	232	**232**	**195**	19	5		0.78
141	2.34	179	**178**	**317**	18	7		0.42
138	2.32	126	**125**	**362**	17	9		0.68
135	2.29	79	**72**	**253**	16	11		0.27
112	2.42	230	**124**	**245**	29	1	(59) E_{55}^S	1.08
111	2.41	200	**126**	**220**	27	5		0.96
110	2.40	176	**118**	**165**	26	7		0.76
108	2.39	146	**110**	**144**	25	9		1.43
107	2.39[a]	116[a]	**90**	**97**	24	11		0.34
105	2.37[a]	87[a]	**76**	**33**	23	13		1.49
103	2.35[a]	61[a]	**59**	**31**	22	15		2.26

[a]Data were obtained using the same model as in Ref. 16.

TABLE II. As Table I but for metallic SWNTs.

ω_{RBM}	E_{ii}	I_{calc}^{max}	I_{calc}^{attn}	I_{meas}^{count}	n	m	Branch	ϵ_{rel} (%)
124.5[a]	2.37	217	**194**	**73**[b]	23	5	(51) E_{33}^M	1.19
123	2.38	170	**142**	**82**	22	7		1.45
122.5[a]	2.37	142	**128**	**121**[b]	21	9		1.11
117	2.33	69	**69**	**185**	19	13		0.01
200	2.28	89	**72**	**17**	15	0	(21) E_{22}^M	0.73
199	2.26	68	**48**	**14**	14	2		0.60
237	2.30	312	**296**	**14**	10	4	(24) E_{11}^M	0.32
228	2.30	157	**147**	**18**	9	6		0.05
277	2.42	636	**338**	**13**	10	1	(21) E_{11}^M	0.41
271	2.50	473	**55**	**10**	9	3		0.19

[a]Tentative assignment.
[b]Averaged data.

very recently[21] and we hereby confirmed their presence which is a direct result of the trigonal warping effect.[22] Regarding further findings, we report on the measurement of even higher metallic transitions, namely, the E_{33}^{M} (or E_{22L}^{M}) transitions. The assignment for these transitions was difficult as the excitation line was spaced equally between the two adjacent tube families (51) and (54) as can be seen in the bottom E_{33}^{M} plot of Fig. 3. The regular and large spacing of the measured peaks comes from the diameter conversion. If $\omega_{RBM} < 110$ cm^{-1}, the resolution in terms of diameter Δd_{min} is on the order of only 0.3 Å. Consequently, only a few transitions could be assigned with reasonable accuracy from the E_{33}^{M} band. Transitions E_{44}^{M} (E_{22H}^{M}) were not recorded. Their tracking with the current methodology is complicated as their calculated Raman intensities are very low.

In conclusion we demonstrated a method of measuring the Raman intensity of a large SWNT population. The data could be matched to calculations of the Raman intensity I_{ii} of individual SWNTs which, in turn, allowed for precise determination of E_{ii} and their related chirality. In total, we identified 28 tubes with a single laser line, excluding tentative assignments. By comparing to the tight-binding calculations we found that the method of obtaining the Raman intensity from a statistical analysis provided more accurate information than the measured intensity itself.

We are grateful to L. Wirtz, B. Babic, M. Height, and J. Meyer for their valuable interaction. A.J. acknowledges financial support from the Swiss National Science Foundation (Grant No. 200021-108059/1) and C.S. acknowledges financial support from ETH Zurich (Grant No. TH-18/03-1).

[1] M. Y. Sfeir *et al.*, Science **312**, 554 (2006).
[2] M. S. Dresselhaus, G. Dresselhaus, A. Jorio, A. G. Souza, and R. Saito, Carbon **40**, 2043 (2002).
[3] S. M. Bachilo, M. S. Strano, C. Kittrell, R. H. Hauge, R. E. Smalley, and R. B. Weisman, Science **298**, 2361 (2002).
[4] M. S. Strano, S. K. Doorn, E. H. Haroz, C. Kittrell, R. H. Hauge, and R. E. Smalley, Nano Lett. **3**, 1091 (2003).
[5] H. Telg, J. Maultzsch, S. Reich, F. Hennrich, and C. Thomsen, Phys. Rev. Lett. **93**, 177401 (2004).
[6] M. J. O'Connell, S. Sivaram, and S. K. Doorn, Phys. Rev. B **69**, 235415 (2004).
[7] H. Kataura, Y. Kumazawa, Y. Maniwa, I. Umezu, S. Suzuki, Y. Ohtsuka, and Y. Achiba, Synth. Met. **103**, 2555 (1999).
[8] J. Maultzsch, H. Telg, S. Reich, and C. Thomsen, Phys. Rev. B **72**, 205438 (2005).
[9] V. N. Popov, L. Henrard, and P. Lambin, Phys. Rev. B **72**, 035436 (2005).
[10] G. S. Duesberg, I. Loa, M. Burghard, K. Syassen, and S. Roth, Phys. Rev. Lett. **85**, 5436 (2000).
[11] C. Fantini, A. Jorio, M. Souza, M. S. Strano, M. S. Dresselhaus, and M. A. Pimenta, Phys. Rev. Lett. **93**, 147406 (2004).
[12] A. Jorio, R. Saito, J. H. Hafner, C. M. Lieber, M. Hunter, T. McClure, G. Dresselhaus, and M. S. Dresselhaus, Phys. Rev. Lett. **86**, 1118 (2001).
[13] A. Jungen, C. Stampfer, J. Hoetzel, V. Bright, and C. Hierold, Sens. Actuators, A **130**, 588 (2006).
[14] J. Kong, H. T. Soh, A. M. Cassell, C. F. Quate, and H. J. Dai, Nature (London) **395**, 878 (1998).
[15] A. Jungen, C. Stampfer, and C. Hierold, Appl. Phys. Lett. **88**, 191901 (2006).
[16] V. N. Popov and L. Henrard, Phys. Rev. B **70**, 115407 (2004).
[17] M. Paillet, T. Michel, J. C. Meyer, V. N. Popov, L. Henrard, S. Roth, and J.-L. Sauvajol, Phys. Rev. Lett. **96**, 257401 (2006).
[18] C. D. Spataru, S. Ismail-Beigi, L. X. Benedict, and S. G. Louie, Phys. Rev. Lett. **92**, 077402 (2004).
[19] E. Chang, G. Bussi, A. Ruini, and E. Molinari, Phys. Rev. Lett. **92**, 196401 (2004).
[20] R. B. Capaz, C. D. Spataru, S. Ismail-Beigi, and S. G. Louie, Phys. Rev. B **74**, 121401(R) (2006).
[21] H. Son, A. Reina, G. G. Samsonidze, R. Saito, A. Jorio, M. S. Dresselhaus, and J. Kong, Phys. Rev. B **74**, 073406 (2006).
[22] R. Saito, G. Dresselhaus, and M. S. Dresselhaus, Phys. Rev. B **61**, 2981 (2000).
[23] Data above 250 cm^{-1} refer to diameters in the tail of the measured diameter distribution which is expanded in the figure because of the $1/d$ conversion.